S1. Supplementary

Blood-wall fluttering instability as a physiomarker for the progression of thoracic aortic aneurysms

Tom Y. Zhao[1,†,*] | PhD, Ethan M.I. Johnson[2,†] | PhD, Guy Elisha[1], Sourav Halder[1], Ben C. Smith [4], Bradley D. Allen [3] | MD, Michael Markl[2,3] | PhD, Neelesh A. Patankar[1,*] | PhD

[1]Northwestern University, Department of Mechanical Engineering: 2145 Sheridan Road, Evanston, Illinois 60208, USA
[2]Northwestern University, Department of Biomedical Engineering: 2145 Sheridan Road, Evanston, Illinois 60208, USA
[3]Northwestern University, Department of Radiology: 676 N St Clair St, Chicago, IL 60611, USA
[4]Northwestern University Feinberg School of Medicine, 420E Superior St, Chicago, IL 60611, USA
[†]These authors contributed equally to this work
[*]Corresponding authors: NAP, TYZ. Emails: n-patankar@northwestern.edu ; tomzhao@u.northwestern.edu

S1.1. **Governing equations - relationship between Womersley number and wall shear.** For a parabolic velocity profile corresponding to Womersley number $w_o = 0$, the wall shear coefficient $\beta = 8$. As w_o increases, the shear contribution becomes localized in a boundary layer at the wall, leading to a larger value of β for higher frequency flow through the blood vessel. Figure S1 presents β normalized by a factor of 8 as w_o varies. The initial nonlinear behavior for $w_o < 2$ smooths out into a linear relation when $w_o > 2$ and the transient inertial forces are large. This relationship spans the full range of physiological heartbeat frequencies.

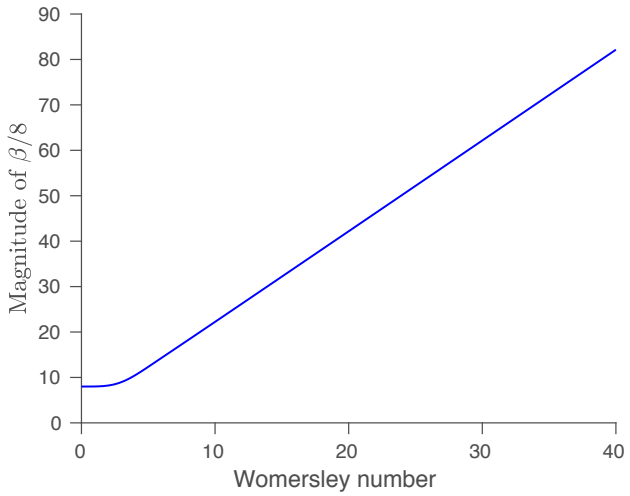

Figure S1. The viscous factor β as a function of Womersley number w_0. Here, β has been normalized by its value at $w_0 = 0$, which corresponds to a parabolic velocity profile.

S1.2. **Pulse wave velocity - relationship with aortic wall stiffness.** The relationship between aortic wall stiffness and pulse wave velocity can be derived by transforming the set of simplified governing equations to the standard form of the wave equation[1]. The relevant conservation equations are

$$\frac{\partial A}{\partial t} + \frac{\partial Au}{\partial x} = 0, \tag{S1}$$

$$\frac{\partial u}{\partial t} + u\frac{\partial u}{\partial x} = -\frac{\partial P}{\partial x}, \tag{S2}$$

where the viscous term has been neglected, and P is the dynamic pressure divided by the blood density. A general tube law is used

$$P = \frac{1}{\rho}G(A), \tag{S3}$$

where G is some function of the local cross-sectional area. The function G represents the full dependence of the excess internal pressure to the cross-sectional area and thus can encapsulate aortic wall properties such as elastic moduli, wall thickness, etc. in the most general case. Without adding new notation, we next introduce an invertible change in the independent variables $x \to x + vt$ and $t \to t$ where the the velocity v is frozen at the mean value. In the new basis, the conservation equations become

$$\frac{\partial A}{\partial t} + A\frac{\partial u}{\partial x} = 0, \tag{S4}$$

$$\frac{\partial u}{\partial t} + \frac{1}{\rho}\frac{\mathrm{d}G}{\mathrm{d}A}\frac{\partial A}{\partial x} = 0. \tag{S5}$$

Differentiating the mass equation (S4) with respect to time and the momentum equation (S5) with respect to space gives

$$\frac{\partial^2 A}{\partial t^2} + A\frac{\partial^2 u}{\partial x \partial t} = 0, \tag{S6}$$

$$\frac{\partial^2 u}{\partial x \partial t} + \frac{1}{\rho}\frac{\mathrm{d}G}{\mathrm{d}A}\frac{\partial^2 A}{\partial x^2} = 0, \tag{S7}$$

which can be combined to obtain

$$\frac{\partial^2 A}{\partial t^2} - \Big(\frac{1}{\rho}\frac{\mathrm{d}G}{\mathrm{d}A}A\Big)\frac{\partial^2 A}{\partial x^2} = 0. \tag{S8}$$

This is the standard form of the wave equation, where the term in parenthesis is typically called the propagation speed. It represents the speed of the plane wave solutions to equation (S8). The pulse wave velocity can thus be defined as

$$c_{pw}^2 = \frac{1}{\rho}\frac{\mathrm{d}G}{\mathrm{d}A}A \tag{S9}$$

S1.3. **Dimensionless groups.** Dimensionless groups are introduced in Table S1. The resulting dimensionless number N_ω captures the dominant physical drivers and inhibitors of the flutter instability.

S1.4. **Cohort criteria.** Here, we present our thoughts on the cohort selection and inclusion / exclusion criteria.

TABLE S1. From the basic variable inputs in the first row, the natural length L and time T scales of the system in the middle row are introduced to produce the dimensionless groups in the last row.

Basic input variables								
ν	ω	R_m	K_e	A_o	u_m	u_ω	ϕ_m	$\bar{\phi}_\omega$
m^2/s	$1/s$	m	$kg/(m \cdot s^2)$	m^2	m/s	m/s	m/s^2	m/s^2
Natural length and time scales of the system								
			$L = \sqrt{A_m}$		$T = \frac{2A_m}{\beta_b \pi \nu}$			
Dimensionless groups								
$\tilde{\mu} = T\mu$	$\tilde{\omega} = T\omega$	$N_T = \frac{K_e {A_m}^2}{\rho A_o (\frac{\beta_b}{2}\pi\nu)^2}$	$k'' = kL\sqrt{N_T}$	$\tilde{A} = \frac{\hat{A}}{L^2}$	$u'' = \frac{\hat{u}T}{L\sqrt{N_T}}$	$N_m = \frac{\phi_m T^2}{L\sqrt{N_T}}$	$N_\omega = \frac{\bar{\phi}_\omega T^2}{L\sqrt{N_T}}$	

S1.5. **Patient cohort.** The patient cohort was drawn from a Radiology Department archive of imaging data and metadata that captures scans from patients who were referred for clinical 4D flow MR imaging. Each record includes the 4D flow MRI of the thoracic aorta, in addition to basic clinical status data (valve type, AS/AR, SOV/MAA diam., EF) and demographic data (age, sex). For some records, the database also includes data files containing the velocity fields and aortic segmentations derived from processing the raw 4D flow images (not all participant data have been processed).

A diverse group of patients was included in the initial cohort formation to allow evaluation of the aneurysm physiomarker across a wider range of patients. The flutter instability parameter's relationship with growth is not specific to a disease type or state; it is derived solely from physical analysis of the blood-wall interaction instability. Therefore, it is not a confound for this study to include patients with different etiology of aortopathy when evaluating general differences relative to a healthy population.

Note that the initial exclusion criteria were structured to avoid known factors for aortic growth (such as aortic stenosis AS or heart failure HF), which could have dominating influence on growth trends by being strong drivers of hemodynamic derangement. Instead, we chose to tackle the more difficult problem by sampling a patient cohort that precluded these overt indicators of growth. Moreover, for exclusion of ejection fraction EF $< 50\%$, only a small number of patients were excluded as a result (less than 15% of all TAV patients, see Fig. S2).

However, in the follow-up subcohort for evaluating prognostic potential for the aneurysm physiomarker, we focused on patients with no genetic tissue disease, etc., as such patients receive a different clinical management regimen than do dilatation patients without such disorders.

S1.6. **Healthy cohort.** The healthy volunteers were recruited as part of a separate study to obtain normative measurements for hemodynamic parameters in healthy participants. A total of 242 healthy participants had been recruited with data available at the time of this study, from which 100 were selected so as to include 10 males and 10 females with no image artifacts in each age grouping of 19-30, 31-40, 41-50, 51-60, and 61-79 years. The selection of 100 participants for analysis was performed by including the first 10 recruited of each sex in each age grouping. For example, if a 38 year-old female was recruited in 2018, but ten females between 31 and 40 years old had already been recruited in 2011-2017, the 2018-recruited 38 year-old female would not be included, while the ten previously-recruited females would be.

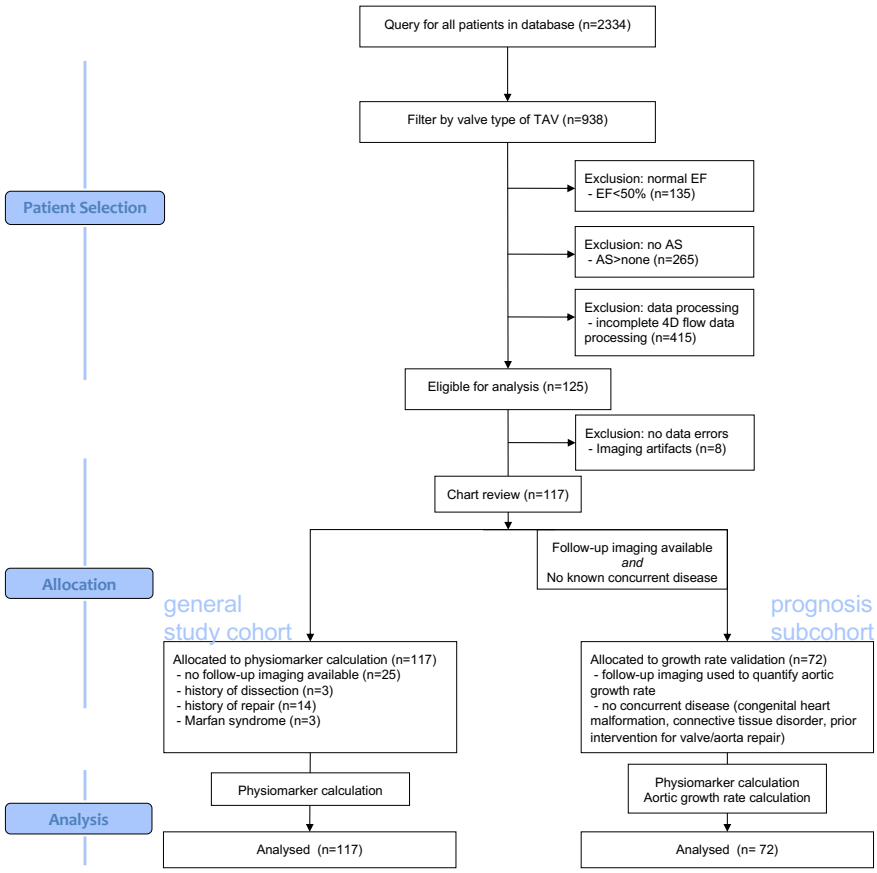

FIGURE S2. A flow diagram for inclusion / exclusion. The diagram reflects a two-stage process for selecting patients, which resulted in the two different analysis groups described in the manuscript. The database was queried to identify patients matching the general inclusion/exclusion criteria (TAV, EV≥50%) with data available for analysis (phase corrections applied to images, aortic segmentation created), thus creating the general cohort of patients. A chart review was conducted to identify patients with no genetic tissue disorders or history of surgical intervention as well as to tabulate aortic dimensions and potential later surgical intervention on follow-up.

Note from Table 2 that the 'healthy' vs 'all aortopathy' cohorts were not age/sex/weight/height matched. As future work, a thorough comparative study with cohort matching should be carried out to validate the proposed aneurysm physiomarker, drawing upon multi-center imaging and follow-up data. The main results of this study are to show that the aneurysm physiomarker is predictive (via follow-up analysis) and that it captures potential growth instabilities that can drive aneurysmal development in healthy participants. In the context of this study, whether the difference in abnormal growth experienced by patient vs healthy participant cohorts arise from differences in age/sex/weight/height is not the focus, since prior work has

been plentiful in showing the trends between aortic aneurysm growth with age/sex/weight/height through statistical correlations.

S1.7. **Image Acquisition and Preprocessing.** Clinical imaging was performed at 1.5T and 3T (Aera / Avanto / Espree, Siemens, Germany). Sequence parameters for 4D flow MRI included 1.2–3.1 × 1.2–3.1 × 1.2–5.0 mm^3 / 33–45 ms spatial / temporal resolution; 12.4–40.6 × 18.0–50.0 × 3.8–17.6 mm^3 field of view; 80–500 cm/s VENC, as appropriate, determined from flow scout image; 2.1–3.0 ms TE, 4.1–5.7 ms TR, 7–25° tip angle; and respiratory navigators for free-breathing scans. Scans for patients used a contrast agent (Ablavar, Magnevist, Multihance), and scans for healthy participants did not. Images for all participants were acquired between January 2011 and December 2019. Pre-processing of 4D flow MRI data included previously-described methods for correction of background phase from eddy currents and Maxwell terms and for velocity phase un-aliasing[2]. Preprocessing was performed with commercial computational software (MATLAB 2019b, 2020b, 2022b, Mathworks, Natick, Massachusetts). Following preprocessing, a three-dimensional phase-contrast MR angiography (3D PCMRA) was generated as a starting point for aortic segmentation by calculating time-averaged velocity sum-of-squares. The 3D PCMRA was then opened in commercial image processing software (Mimics Innovation Suite v. 20.0.0.691, Materialize, Leuven, Belgium) along with magnitude images and edited to remove errant inclusions or add missed sections of the aorta.

Note that we did not find any significant difference in acquisition parameters such as magnetic field strength, flip angle, pixel bandwidth, echo time, repetition time, slice thickness, VENC, spatial resolution, temporal resolution, etc. ($p>0.2$) between patients with abnormal vs low growth as defined by the aneurysm physiomarker $N_{\omega,\mathrm{sp}} > 0$ and vice versa. This statistical comparison was done with the Wilcoxon rank sum test. Likewise, there was also no significant difference between high vs low growth patients in use or non-use of contrast agents ($p=0.9$).

S1.8. **Image Processing.** The 4D flow MRI provides information about the three-dimensional geometry of the aorta as well as the velocity field inside it. The 3D geometry is time-averaged from velocity contrast, and therefore remains constant in time. Fig. S3(a) shows the time-averaged geometry of an aorta from a 4D flow MRI. The geometry is generated on a Cartesian grid of voxels which have a binary value, i.e., voxels lying outside and inside the aorta have a value of 0 and 1, respectively. The measured velocity field is a function of both space and time.

Our analysis was focused only on the ascending aorta, from the aortic root to just below the three branches at the aortic arch. This region is shown inside the red box in Fig. S3 (a) and more clearly zoomed in Fig. S3(b). The upper and lower limits of the ascending aorta were segmented manually.

To model the ascending part of the aorta in a one-dimensional model, we find the variation of cross-sectional area and mean velocity along its length. A centerline is first generated through the ascending aorta (Fig. S3(b)). Normal planes are then generated. These planes were used to calculate the cross-sectional areas and mean velocities at every point along the centerline. Voxels on each plane are then meshed using Delaunay triangulation (Fig. S3(c)). The sum of these triangles is the cross-sectional area A_m of the aorta at a particular centerpoint.

The mean velocity at each cross-section are calculated by

$$u(x,t) = \frac{1}{N}\sum_{i}^{N} \mathbf{v}_i(x,t)\cdot\hat{\mathbf{n}}, \tag{S10}$$

where u is the mean velocity at the centerline, i represents the i-th point in plane, N is the total number of points, $\mathbf{v}_i$ is the velocity at the i-th point, $\hat{\mathbf{n}}$ is the unit normal to the plane, x is the distance along the centerline, and t is time. The variation of $u(x,t)$ during a cardiac cycle is shown in Fig. S3(d).

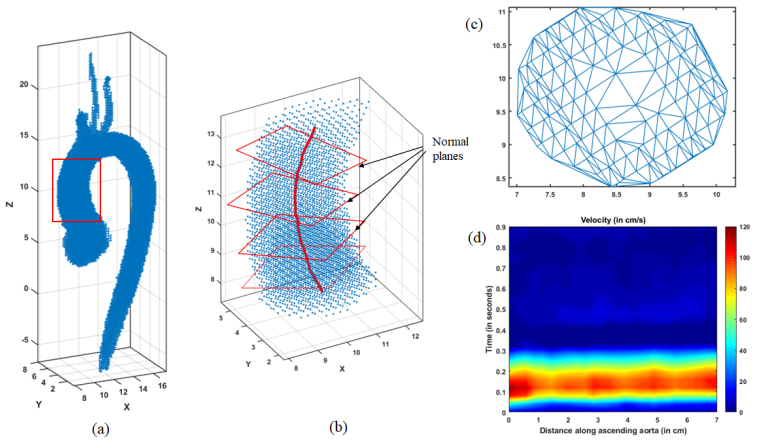

FIGURE S3. Cross-sectional areas and mean velocity field from 4D flow MRI of the aorta. (a) Time-averaged 3D geometry of the aorta. The red box marks the ascending aorta. The axes units are in cm; (b) Point cloud (in blue) showing the ascending aorta. The red curve shows the centerline, and the red boxes show the planes normal to the centerline. These planes are used to calculate the cross-sectional areas and mean velocities. The axes units are in cm; (c) An example of the aorta cross-section on a normal plane. Meshing is done using Delaunay triangulation to calculate the cross-sectional area at the normal plane. The axes units are in cm; (d) Variation of mean velocity as a function of time and length along the ascending aorta.

These velocity profiles can be used to calculate the pressure gradient that drives oscillatory blood acceleration $\bar{\phi}_\omega$ via equation (10) as well as the pressure gradient that drives the mean blood acceleration ϕ_m via $u_m = \frac{\phi_m A_m}{\beta_m \pi \nu}$. The pulse wave velocity c_{pw} is also found from the velocity profiles $u(x,t)$ using the cross correlation (XCor)[3] method, which agrees with literature values for healthy controls and patients[5]. Briefly, the XCor PWV value is calculated by automated placement of a centerline in the aortic segmentation and creation of analysis planes every 4mm along the length, then cross-correlating the through-plane flow-time curves to find the transit time between all locations of the aorta[6;7]. The heartbeat frequency ω is used to calculate the Womersley number $w_0 = R\sqrt{\omega/\nu} \geq 0$ and then the friction coefficient β_b from equation (9). The remaining parameters of kinematic viscosity ν and density ρ of blood used to determine $N_{\omega,\text{sp}}$ were sourced from reference values in literature ($\nu \approx 4e-3\text{N s/m}^2$ and $\rho \approx 1060\ \text{kg/cm}^3$)[8]

S1.9. **Age & sex dependencies of the aneurysm physiomarker.** Table S2 shows that the distribution of the aneurysm physiomarker among different sex and age groups in the two cohorts appear to agree with general population trends reported in the literature.

	$N_{\omega,\mathrm{sp}}$		
	Age < 40	$40 \leq$ Age < 60	Age ≥ 60
Patients			
median (female)	2.8590	0.3372	-0.1557
p-value between sexes	0.0531	0.1837	0.3264
p-value (female) between age groups	**0.0388**	0.1764	**0.0091**
p-value (female) between cohorts	**0.0042**	0.0952	**0.0227**
median (male)	0.3330	-0.1027	-0.0963
p-value (male) between age groups	0.1002	0.4582	0.1043
p-value (male) between cohorts	0.4571	0.2944	**0.0150**
Normal participants			
median (female)	-0.1244	-0.0660	-0.6831
p-value between sexes	**0.0122**	0.3276	0.4849
p-value (female) between age groups	0.4037	$\mathbf{6 \times 10^{-4}}$	**0.0018**
median (male)	0.7286	-0.1000	-0.8908
p-value (male) between age groups	**0.0019**	**0.0080**	$\mathbf{3 \times 10^{-4}}$

TABLE S2. The aneurysm physiomarker $N_{\omega,\mathrm{sp}}$ stratified by age and sex. The one-tailed Wilcoxon rank sum test was used to determine whether the larger median of one population (e.g. patients, Age < 40, female) is significantly greater than the smaller median of the other (e.g. normal participants, Age < 40, female). The p-values comparing patient and normal participant cohorts; the p-values comparing sexes; and the p-values comparing each age group are presented. Note that the p-value beneath Age < 40 tests the age groups Age < 40 and $40 \leq$ Age < 60, the p-value beneath $40 \leq$ Age < 60 tests the age groups $40 \leq$ Age < 60 and $40 \leq$ Age, and the p-value beneath Age ≥ 60 tests the age groups Age ≥ 60 and Age < 40. Rejection of the null hypothesis at the 5% level is in bold.

S1.10. **The changes in aortic wall compliance during aneurysm development.** Changes in aortic wall stiffness has been shown in the literature to determine the trajectory of aneurysm progression, as shown in Table S3. Specifically, wall stiffening appears to result in stable aneurysms that do not exhibit increased risk of rupture or significant growth (Type 1), while compliant walls are associated with unstable aneurysms that are at increased risk of further abnormal dilatation and rupture (Type 2).

TABLE S3. Summary of relevant published literature on the role of aortic wall distensibility in aneurysm progression and rupture.

Aneurysm studied	Method/modality	Summary of findings	Author/year
AAA	112 patients with initially non-operated AAA were recruited from five centres. They underwent baseline compliance measurements and were then followed for a median of 7 months.	• Comparing AAA of similar sizes, AAA which rupture or require elective repair appear to be more compliant than those AAA that do not. • Aneurysms can be classified into two types (**a**) Type I - further enlargement is accompanied by increasing stiffness from increased collagen deposition and/or remodelling in the aortic wall. This confers strength to the AAA so that the risk of rupture is low. • (**b**) Type II - further enlargement is not associated with an increasing stiffness, and stiffness may even fall. This can result from a failure to lay down and remodel collagen, leading to weak or "thinning" aortic walls. These aneurysms are at risk of rupture.	Wilson et. al (1998)[9]
AAA	62 males of median age 68 with detected AAA were screened for circulating markers of elastin and collagen metabolism	• Increased elastolysis- which induces media degradation and leads to aneurysm rupture- is associated with increasing distensibility of the aortic wall • Most aneurysms become less distensible as they expand; those that fail to grow stiffer or become suddenly more distensible are at high risk of rupture. • The change in distensibility within each aneurysm is of greater significance than differences between a level of “normal” distensibility and that of the aneurysm.	Wilson et. al (2001)[10]

AAA	A prospective, six-center study of 210 patients with AAA was conducted. Blood pressure (BP), maximum AAA diameter (Dmax), and AAA distensibility (pressure strain elastic modulus Ep) were measured at 6 months with an ultrasound scan–based echo-tracking technique.	• The reduction in AAA distensibility over time is associated with a significantly shorter time to rupture, independent of other risk factors (age, sex, BP, Dmax).	Wilson et. al (2003) [11]
AAA	A prospective study of 56 patients with AAA was conducted using tissue Doppler imaging system.	• There is a significant positive relationship between maximum diameter and the segmental compliance of the aneurysm. • When stratified by size into two groups (group 1, AAA diameter $<$ 45 mm and group 2, AAA diameter $\geq$ 45 mm), group 2 had significantly higher segmental compliance while group 1 exhibited greater scatter in stiffness.	Long et. al (2005) [12]
AAA	A study of 43 patients with infrarenal AAAs was conducted in the postoperative period	• Patients with electively repaired AAAs have accelerated pulse wave velocities, indicating highly rigid aortic walls. • Patients with ruptured aneurysms exhibited significantly lower pulse wave velocities with greater variance and scatter. • Patients with high aortic compliance experience faster growth and earlier rupture.	Russo (2006) [13]
TAA	A study of 32 patients with ascending TAAs and 46 age matched controls was conducted to measure the femoral pulse wave velocity (cfPWV), heart-femoral pulse wave velocity (hfPWV) and brachial-ankle pulse wave velocity (baPWV)	• In patients with ascending TAAs, there was a significant inverse relationship between aortic diameter at the SOV and cfPWV, as well as hfPWV, but not with baPWV. This correlation was not present in controls without ascending TAA.	Rabkin et. al (2014) [14]

TAA	A study of 40 patients with TAAs was conducted to measure regional aortic diameter and PWV using 1.5 T MRI	• Incidence of increased regional PWV exhibited moderate specificity but low sensitivity for coexisting with regional aortic dilatation in the ascending aorta and aortic arch.	Kröner et. al (2015)[15]
AAA	Biaxial extension tests, second-harmonic generation imaging and histology were performed on 15 samples from the anterior part of AAA walls harvested during open aneurysm surgery.	• Three stages of disease progression were identified. (**a**) Stage 1 - intimal thickening is accompanied by a decrease in elastin and smooth muscle cell (SMC) content. Stiffness decreased by a factor of 2 compared to a healthy aorta. • (**b**) Stage 2 - Further decrease in elastin and SMC content along with increase in adipocytes in the wall. A neo-adventitia layer formed from new collagen deposition on the outer AAA walls, which did not appear in healthy or stage 1 participants. Wall distensibility increases compared to healthy or stage 1 AAA participants. . • (**b**) Stage 3 - Significant buildup of neo-adventitia occurs along with media and intima breakdown. Two types of stage 3 walls were observed. Type 1 AAA had 'safely' remodeled walls with no adipocytes present in the wall and a thick collagen layer. Type 2 AAA remodeled to a 'vulnerable' state, exhibiting significant inflammation and adipocytes inside the wall.	Niestrawska et. al (2019)[16]

S1.11. **Aneurysm physiomarker trend with patient increased growth rates.** Fig. S4 demonstrates a positively proportional relationship between the increasing aneurysm physiomarker N_ω and greater growth rates in the SOV and MAA. The correlation coefficient between Δ SOV_{max} and the aneurysm physiomarker is 0.56, with a p-value of 4×10^{-7}, whereas the correlation coefficient between Δ MAA_{max} and the aneurysm physiomarker is 0.58, with a p-value of 8×10^{-8}.

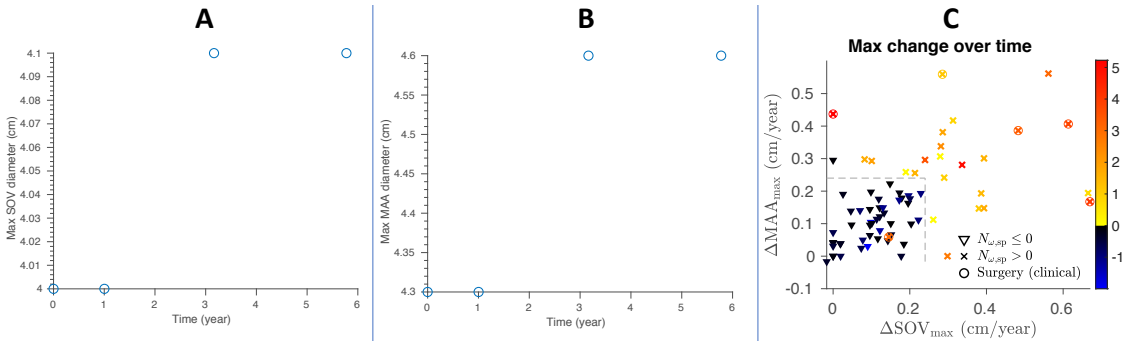

FIGURE S4. **A**) Example of the maximum SOV diameter recorded during each clinical visit for one patient. **B**) Example of the maximum MAA diameter recorded during each clinical visit for one patient. **C**) A prediction vs outcome diagram of all patients with follow-up imaging data. The maximum growth rate of their MAA and SOV in (cm/year) are simultaneously visualized by color with respect to the magnitude of $N_{\omega,\mathrm{sp}}$. $N_{\omega,\mathrm{sp}}$ is calculated from an MRI at time zero. If $N_{\omega,\mathrm{sp}} > 0$, the patient's marker is labeled by x's. Otherwise, the data point is labeled by downward pointing triangles. The circles indicate that the patient experienced a surgical intervention after their initial MRI at year 0. $N_{\omega,\mathrm{sp}} > 0$ appears to correlate with larger growth rates for the MAA and SOV. The growth threshold of 0.24 cm/year is labeled by black dotted lines- this value is outside the normal range of growth in TAAs of all sizes[17] (< 0.2 cm/year) and optimally discriminates between stable and unstable aneurysms predicted by the proposed aneurysm physiomarker. This optimal threshold of 0.24 cm/year falls within the clinically observed range of abnormal growth (0.24 cm/year for small aneurysms to 0.31 cm/year or large aneurysms) that is associated with chronic dissection.

S1.12. **Additional limitations.** We estimate the sensitivity of the aneurysm physiomarker performance to uncertainty in the input physiological terms. By using the aortic growth rate of 0.24 cm/year as an indicator of significant growth, the aneurysm physiomarker $N_{\omega,\mathrm{sp}} > 0$ serves as a good binary predictor for the growth outcome of each patient. The area under the curve (AUC) of a receiver operating characteristic (ROC) analysis is 0.997 for the unaltered input parameters and 0.994 for a 5% variation of the input parameters around their measured or assumed constant value (e.g. kinematic viscosity of blood).

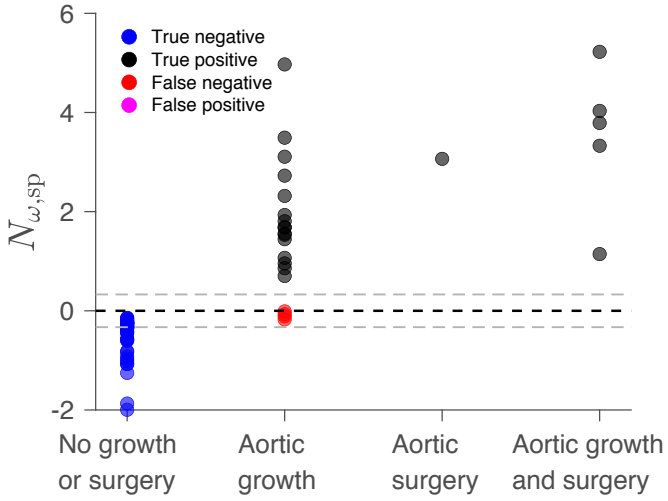

FIGURE S5. After varying each input parameter independently by 5% around their measured or assumed constant value (kinetmatic viscosity), the largest resulting change in the aneurysm physiomarker which pushes $N_{\omega,\mathrm{sp}}$ toward the opposite sign is plotted. Each patient has been labeled according to whether $N_{\omega,\mathrm{sp}} > 0$ accurately predicts a growth outcome, categorized as exhibiting a growth rate in SOV or MAA $\geq$ 0.24 cm/year or experiencing surgical intervention at follow-up. A 5% change in the input parameters can induce at maximum a difference of 0.33 in the aneurysm physiomarker $N_{\omega,\mathrm{sp}}$; this uncertainty band has been labeled by the grey dotted lines around the marginal stability threshold of $N_{\omega,\mathrm{sp}} = 0$. That is, $N_{\omega,\mathrm{sp}}$ which fall in this band of ± 0.33 are sensitive (may swing between positive and negative values) to errors in the measurement of the physiological input parameters, such as pulse wave velocity. Repeat imaging and more frequent clinical follow-ups are therefore recommended to accurately quantify the physiomarker and predict future abnormal growth.

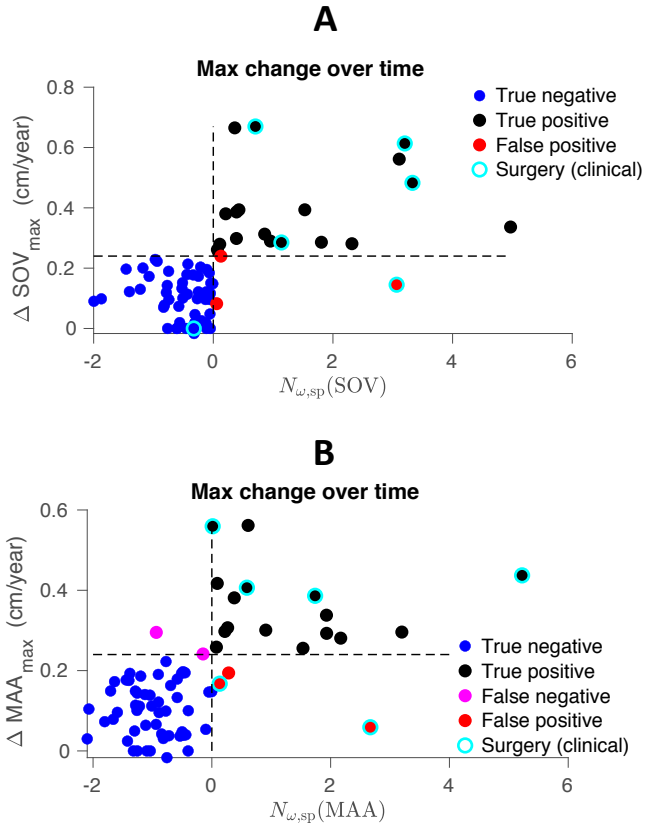

FIGURE S6. **A**) The growth rate at the SOV vs the local aneurysm physiomarker, defined as the maximum $N_{\omega,\mathrm{sp}}$ along the beginning 20% of the ascending thoracic aorta (truncated before the arch). **B**) The growth rate at the MAA vs the local aneurysm physiomarker, defined as the maximum $N_{\omega,\mathrm{sp}}$ along the middle 40% to 60% of the ascending thoracic aorta (truncated before the arch). The dotted line plotted vertically on the x-axis is at 0, denoting the marginal stability of $N_{\omega,\mathrm{sp}} = 0$. The dotted line plotted horizontally on the y-axis is at 0.24 cm/year, the empirically found growth threshold that optimally discriminates between stable and unstable aneurysms predicted by the proposed aneurysm physiomarker.

S1.13. **Growth in SOV and MAA vs local aneurysm physiomarker.**

S1.14. **ROC analysis.** The optimal cut-off was found as the point where the ROC curve crosses a straight line with slope g, such that

$$g = \frac{\text{costfn}(P|N) - \text{costfn}(N|N)}{\text{costfn}(N|P) - \text{costfn}(P|P)} \frac{y}{x}. \tag{S11}$$

Here, x is the number of observations in the positive classification, and y is the total number of observations in the negative classification. The cost function gives components of the matrix B

$$B = \begin{bmatrix} \text{costfn}(P|P) & \text{costfn}(N|P) \\ \text{costfn}(P|N) & \text{costfn}(N|N) \end{bmatrix} = \begin{bmatrix} 0 & 1 \\ 1 & 0 \end{bmatrix}, \tag{S12}$$

where costfn(N|P) is the cost of misclassifying a positive classification as a negative classification and vice versa. The optimal operating point is found at the intersection of the straight line with slope m from the upper left corner of the ROC plot (sensitivity=specificity=1) and the ROC curve.

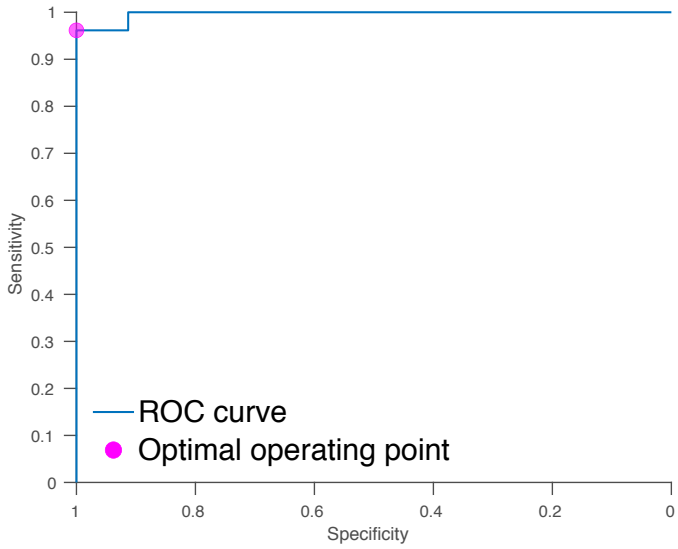

FIGURE S7. The receiver operating characteristic (ROC) analysis curve, plotted as sensitivity vs. specificity across varying cutoffs of $N_{\omega,\text{sp}}$. The optimal operating point[18] (sensitivity = 0.96, specificity = 1) occurs at the $N_{\omega,\text{sp}} = 0.07 \approx 0$ for patients with follow-up data, suggesting that the analytically derived threshold $N_{\omega,\text{threshold}}$ accurately describes the onset of the underlying instability.

S1.15. **Establishing the marginal stability curve.** From the characteristic equations 22 and 23, we can determine the marginal stability curve where $\tilde{\mu} = 0$ via the method proposed by Kumar et al[19]. The measurable values of k'', $\tilde{\omega}$, and N_m are fixed for a specific flow scenario, yielding an eigenvalue problem for the critical $N_{\omega,\text{threshold}}$ associated with $\tilde{\mu} = 0$.

We first write our solution set of Fourier coefficients $\tilde{A}_{k,n} = \tilde{A}^r_{k,n} + i\tilde{A}^i_{k,n}$, $u''_{k,n} = u''^r_{k,n} + iu''^i_{k,n}$ in terms of real and imaginary components. Then the dimensionless characteristic equations 22 and 23 can likewise be separated into purely real and imaginary parts

Mass equation

$$\begin{aligned}
&\tilde{A}^r_{k,n}\mu + \tilde{A}^i_{k,n}\left(-\tilde{\omega}(\alpha+n) - \frac{k''N_m}{2}\right) + \frac{\tilde{A}^r_{k,n-1}k''N_\omega(2\text{ph}[\beta_b]^i + \tilde{\omega})}{8\text{ph}[\beta_b]^{r2} + 2(2\text{ph}[\beta_b]^i + \tilde{\omega})^2} \\
&+\frac{\tilde{A}^r_{k,n+1}k''N_\omega(2\text{ph}[\beta_b]^i - \tilde{\omega})}{8\text{ph}[\beta_b]^{r2} + 2(\tilde{\omega} - 2\text{ph}[\beta_b]^i)^2} - \frac{\tilde{A}^i_{k,n-1}\text{ph}[\beta_b]^r k''N_\omega}{4\text{ph}[\beta_b]^{r2} + (2\text{ph}[\beta_b]^i + \tilde{\omega})^2} \\
&-\frac{\tilde{A}^i_{k,n+1}\text{ph}[\beta_b]^r k''N_\omega}{4\text{ph}[\beta_b]^{r2} + (\tilde{\omega} - 2\text{ph}[\beta_b]^i)^2} - k''u''^i_{k,n} \\
+i\Bigg(&\tilde{A}^r_{k,n}\left(\tilde{\omega}(\alpha+n) + \frac{k''N_m}{2}\right) + \frac{\tilde{A}^r_{k,n-1}\text{ph}[\beta_b]^r k''N_\omega}{4\text{ph}[\beta_b]^{r2} + (2\text{ph}[\beta_b]^i + \tilde{\omega})^2} + \frac{\tilde{A}^r_{k,n+1}\text{ph}[\beta_b]^r k''N_\omega}{4\text{ph}[\beta_b]^{r2} + (\tilde{\omega} - 2\text{ph}[\beta_b]^i)^2} \\
&+\tilde{A}^i_{k,n}\mu + \frac{\tilde{A}^i_{k,n-1}k''N_\omega(2\text{ph}[\beta_b]^i + \tilde{\omega})}{8\text{ph}[\beta_b]^{r2} + 2(2\text{ph}[\beta_b]^i + \tilde{\omega})^2} + \frac{\tilde{A}^i_{k,n+1}k''N_\omega(2\text{ph}[\beta_b]^i - \tilde{\omega})}{8\text{ph}[\beta_b]^{r2} + 2(\tilde{\omega} - 2\text{ph}[\beta_b]^i)^2} + k''u''^r_{k,n}\Bigg) = 0,
\end{aligned} \tag{S13}$$

Momentum equation

$$\begin{aligned}
&-\frac{\tilde{A}^r_{k,n}\beta_m N_m}{|\beta_b|} + u''^i_{k,n}\left(-\frac{2\beta^i_p}{|\beta_b|} - \tilde{\omega}(\alpha+n) - \frac{k''N_m}{2}\right) + u''^r_{k,n}\left(\frac{2\beta^r_p}{|\beta_b|} + \mu\right) \\
&-\frac{\tilde{A}^r_{k,n-1}N_\omega\left(2\text{ph}[\beta_b]^{r2} + \text{ph}[\beta_b]^i(2\text{ph}[\beta_b]^i + \tilde{\omega})\right)}{4\text{ph}[\beta_b]^{r2} + (2\text{ph}[\beta_b]^i + \tilde{\omega})^2} + \frac{\tilde{A}^r_{k,n+1}N_\omega\left(\text{ph}[\beta_b]^i\tilde{\omega} - 2\left(c^2+d^2\right)\right)}{4\text{ph}[\beta_b]^{r2} + (\tilde{\omega} - 2\text{ph}[\beta_b]^i)^2} - \tilde{A}^i_{k,n}k \\
&-\frac{\tilde{A}^i_{k,n-1}\text{ph}[\beta_b]^r N_\omega\tilde{\omega}}{4\text{ph}[\beta_b]^{r2} + (2\text{ph}[\beta_b]^i + \tilde{\omega})^2} + \frac{\tilde{A}^i_{k,n+1}\text{ph}[\beta_b]^r N_\omega\tilde{\omega}}{4\text{ph}[\beta_b]^{r2} + (\tilde{\omega} - 2\text{ph}[\beta_b]^i)^2} + \frac{k''N_\omega u''^r_{k,n-1}(2\text{ph}[\beta_b]^i + \tilde{\omega})}{8\text{ph}[\beta_b]^{r2} + 2(2\text{ph}[\beta_b]^i + \tilde{\omega})^2} \\
&+\frac{k''N_\omega u''^r_{k,n+1}(2\text{ph}[\beta_b]^i - \tilde{\omega})}{8\text{ph}[\beta_b]^{r2} + 2(\tilde{\omega} - 2\text{ph}[\beta_b]^i)^2} - \frac{\text{ph}[\beta_b]^r k''N_\omega u''^i_{k,n-1}}{4\text{ph}[\beta_b]^{r2} + (2\text{ph}[\beta_b]^i + \tilde{\omega})^2} - \frac{\text{ph}[\beta_b]^r k''N_\omega u''^i_{k,n+1}}{4\text{ph}[\beta_b]^{r2} + (\tilde{\omega} - 2\text{ph}[\beta_b]^i)^2} \\
&+i\Bigg(\tilde{A}^r_{k,n}k + u''^r_{k,n}\left(\frac{2\beta^i_p}{|\beta_b|} + \tilde{\omega}(\alpha+n) + \frac{k''N_m}{2}\right) - \frac{\tilde{A}^i_{k,n}\beta_m N_m}{|\beta_b|} + u''^i_{k,n}\left(\frac{2\beta^r_p}{|\beta_b|} + \mu\right) \\
&+\frac{\tilde{A}^r_{k,n-1}\text{ph}[\beta_b]^r N_\omega\tilde{\omega}}{4\text{ph}[\beta_b]^{r2} + (2\text{ph}[\beta_b]^i + \tilde{\omega})^2} - \frac{\tilde{A}^r_{k,n+1}\text{ph}[\beta_b]^r N_\omega\tilde{\omega}}{4\text{ph}[\beta_b]^{r2} + (\tilde{\omega} - 2\text{ph}[\beta_b]^i)^2} \\
&-\frac{\tilde{A}^i_{k,n-1}N_\omega\left(2\text{ph}[\beta_b]^{r2} + \text{ph}[\beta_b]^i(2\text{ph}[\beta_b]^i + \tilde{\omega})\right)}{4\text{ph}[\beta_b]^{r2} + (2\text{ph}[\beta_b]^i + \tilde{\omega})^2} + \frac{\tilde{A}^i_{k,n+1}N_\omega\left(\text{ph}[\beta_b]^i\tilde{\omega} - 2\left(c^2+d^2\right)\right)}{4\text{ph}[\beta_b]^{r2} + (\tilde{\omega} - 2\text{ph}[\beta_b]^i)^2} \\
&+\frac{\text{ph}[\beta_b]^r k''N_\omega u''^r_{k,n-1}}{4\text{ph}[\beta_b]^{r2} + (2\text{ph}[\beta_b]^i + \tilde{\omega})^2} + \frac{\text{ph}[\beta_b]^r k''N_\omega u''^r_{k,n+1}}{4\text{ph}[\beta_b]^{r2} + (\tilde{\omega} - 2\text{ph}[\beta_b]^i)^2} \\
&+\frac{k''N_\omega u''^i_{k,n-1}(2\text{ph}[\beta_b]^i + \tilde{\omega})}{8\text{ph}[\beta_b]^{r2} + 2(2\text{ph}[\beta_b]^i + \tilde{\omega})^2} + \frac{k''N_\omega u''^i_{k,n+1}(2\text{ph}[\beta_b]^i - \tilde{\omega})}{8\text{ph}[\beta_b]^{r2} + 2(\tilde{\omega} - 2\text{ph}[\beta_b]^i)^2}\Bigg) = 0,
\end{aligned} \tag{S14}$$

where $\text{ph}[\beta_b] = \text{ph}[\beta_b]^r + i\text{ph}[\beta_b]^i$ and $\beta_b = \beta_b^r + i\beta_b^i$. The real and imaginary parts of equation (S13) as well as S14 must each be identically zero to fully satisfy both characteristic equations. This provides four equations for four unknowns, $\underline{Z} = [\tilde{A}_{k,n}^r, \tilde{A}_{k,n}^i, u_{k,n}''^r, u_{k,n}''^i]'$, which can be written as a linear equation $\boldsymbol{J}\underline{Z} = 0$. The matrix $\boldsymbol{J}$ thus comprises the linear coefficients of $\underline{Z}$ in the real & imaginary parts of the mass (equation (S13)) and momentum (equation (S14)) equations.

The real part of the temporal growth rate is set to $\tilde{\mu} = 0$. The imaginary part takes on the value $\alpha = 1/2$ for the subharmonic resonance in which the response frequency is half the driving frequency, and $\alpha = 0$ for the harmonic case where the response frequency is the same as the driving frequency $\tilde{\omega}$. Since integer multiples of $\tilde{\omega}$ can be absorbed into the periodic function $\boldsymbol{P}(t)$, α is defined modulo $\tilde{\omega}$. The Fourier terms with $0 < \alpha < 1/2$ is equivalent to the complex conjugate terms associated with $1/2 < \alpha < 1$, so consideration can be restricted to $0 \leq \alpha \leq 1/2$. However, we note that $0 < \alpha < 1/2$ are only associated with stable flows $\tilde{\mu} \leq 0$ in the range of physiologically viable N_ω [19]. Kumar et al. showed in their analogous analysis of an interface between two fluids that only the harmonic and subharmonic cases are relevant to the linear stability problem. The complex Floquet multipliers associated with $0 \leq \alpha \leq 1/2$ correspond to damped, stable solutions. We have verified that this holds true for selected α in the range $0 \leq \alpha \leq 1/2$ for physiologically viable N_ω, though a rigorous theoretical proof remains an open problem.

The critical $N_{\omega,\text{crit}}$ corresponding to the marginal stability curve $\tilde{\mu} = 0$ as well as the k'', $\tilde{\omega}$, and N_m selected for a specific flow scenario can be found by solving an eigenvalue problem. Specifically, we decompose $\boldsymbol{J}$ into $\boldsymbol{C}$, the linear coefficients of $\underline{Z}$ in $\boldsymbol{J}$ that do not contain N_ω, and $\boldsymbol{D}$, the entries of $\boldsymbol{J}$ that are proportional to N_ω. The linear matrix equation becomes

$$\boldsymbol{C}\underline{Z} + N_\omega \boldsymbol{D}\underline{Z} = 0. \tag{S15}$$

This can be written as an eigenvalue problem

$$-\text{inv}(\boldsymbol{C})\boldsymbol{D}\underline{Z} = \frac{1}{N_{\omega,\text{crit}}}\underline{Z}, \tag{S16}$$

where the eigenvalues of the matrix $-\text{inv}(\boldsymbol{C})\boldsymbol{D}$ are reciprocals of the critical $N_{\omega,\text{crit}}$ on the marginal stability curve. The preset values of $\tilde{\omega}$ and N_m are measured from patient MRI, and k'' is swept through to obtain the "tongues" observed in Fig. 2. The minimum critical N_ω associated with the first subharmonic tongue to appear as k'' increases is chosen as the threshold $N_{\omega,\text{threshold}}$. It is the global minimum of $N_{\omega,\text{crit}}$ on all marginal stability tongues, such that the flutter instability is triggered first for increasing N_ω at the value $N_{\omega,\text{threshold}}$.

References

[1] Y. Ma, J. Choi, A. Hourlier-Fargette, Y. Xue, H. U. Chung, J. Y. Lee, X. Wang, Z. Xie, D. Kang, H. Wang, S. Han, S.-K. Kang, Y. Kang, X. Yu, M. J. Slepian, M. S. Raj, J. B. Model, X. Feng, R. Ghaffari, J. A. Rogers, and Y. Huang. Relation between blood pressure and pulse wave velocity for human arteries. *Proceedings of the National Academy of Sciences*, 115(44):11144, 10 2018.

[2] J. Bock, B. Kreher, J. Hennig, and M. Markl. Optimized pre-processing of time-resolved 2d and 3d phase contrast mri data. In *Proceedings of the 15th Annual meeting of ISMRM, Berlin, Germany*, page 3138, Berlin, Federal Republic of Germany, 2007.

[3] M. Markl, W. Wallis, S. Brendecke, J. Simon, A. Frydrychowicz, and A. Harloff. Estimation of global aortic pulse wave velocity by flow-sensitive 4d mri. *Magnetic Resonance in Medicine*, 63(6):1575–1582, 2022/08/22 2010.

[4] M. Markl, W. Wallis, C. Strecker, B. P. Gladstone, W. Vach, and A. Harloff. Analysis of pulse wave velocity in the thoracic aorta by flow-sensitive four-dimensional mri: Reproducibility and correlation

with characteristics in patients with aortic atherosclerosis. *Journal of Magnetic Resonance Imaging*, 35(5):1162–1168, 2022/08/22 2012.

[5] R. V. for Arterial Stiffness' Collaboration. Determinants of pulse wave velocity in healthy people and in the presence of cardiovascular risk factors: 'establishing normal and reference values'. *Eur Heart J*, 31(19):2338–2350, Oct 2010.

[6] K. Jarvis, G. Soulat, M. Scott, A. Vali, A. Pathrose, A. A. Syed, M. Kinno, S. Prabhakaran, J. D. Collins, and M. Markl. Investigation of Aortic Wall Thickness, Stiffness and Flow Reversal in Patients With Cryptogenic Stroke: A 4D Flow MRI Study. *Journal of Magnetic Resonance Imaging*, 53(3):942–952, August 2020.

[7] E. M. Johnson, M. B. Scott, K. Jarvis, B. Allen, J. Carr, S. C. Malaisrie, P. McCarthy, C. Mehta, P. W. Fedak, A. J. Barker, and M. Markl. Global Aortic Pulse Wave Velocity is Unchanged in Bicuspid Aortopathy With Normal Valve Function but Elevated in Patients With Aortic Valve Stenosis: Insights From a 4D Flow MRI Study of 597 Subjects. *Journal of Magnetic Resonance Imaging*, page jmri.28266, May 2022.

[8] S. Aslan, P. Mass, Y.-H. Loke, L. Warburton, X. Liu, N. Hibino, L. Olivieri, and A. Krieger. Non-invasive prediction of peak systolic pressure drop across coarctation of aorta using computational fluid dynamics. *Annual International Conference of the IEEE Engineering in Medicine and Biology Society. IEEE Engineering in Medicine and Biology Society. Annual International Conference*, 2020:2295–2298, 07 2020.

[9] K. Wilson, A. Bradbury, M. Whyman, P. Hoskins, A. Lee, G. Fowkes, P. McCollum, and C. Vaughan Ruckley. Relationship between abdominal aortic aneurysm wall compliance and clinical outcome: a preliminary analysis. *European Journal of Vascular and Endovascular Surgery*, 15(6):472–477, 1998.

[10] K. A. Wilson, J. S. Lindholt, P. R. Hoskins, L. Heickendorff, S. Vammen, and A. W. Bradbury. The relationship between abdominal aortic aneurysm distensibility and serum markers of elastin and collagen metabolism. *European Journal of Vascular and Endovascular Surgery*, 21(2):175–178, 2001.

[11] K. A. Wilson, A. J. Lee, A. J. Lee, P. R. Hoskins, F. G. R. Fowkes, C. V. Ruckley, and A. W. Bradbury. The relationship between aortic wall distensibility and rupture of infrarenal abdominal aortic aneurysm. *Journal of Vascular Surgery*, 37(1):112–117, 2003.

[12] A. Long, L. Rouet, A. Bissery, P. Rossignol, D. Mouradian, and M. Sapoval. Compliance of abdominal aortic aneurysms evaluated by tissue doppler imaging: Correlation with aneurysm size. *Journal of Vascular Surgery*, 42(1):18–26, 2005.

[13] L. Russo. Thoracic aortic compliance as a determinant of rupture of abdominal aortic aneurysms. *Annals of the New York Academy of Sciences*, 1085(1):363–366, 2022/08/22 2006.

[14] S. W. Rabkin, K. K. Chan, B. Chow, and M. T. Janusz. Pulse wave velocity involving proximal portions of the aorta correlates with the degree of aortic dilatation at the sinuses of valsalva in ascending thoracic aortic aneurysms. *Ann Vasc Dis*, 7(4):404–409, 2014.

[15] E. S. J. Kröner, J. J. M. Westenberg, L. J. M. Kroft, N. J. Brouwer, P. J. van den Boogaard, and A. J. H. A. Scholte. Coupling between mri-assessed regional aortic pulse wave velocity and diameters in patients with thoracic aortic aneurysm: a feasibility study. *Neth Heart J*, 23(10):493–501, Sep 2015.

[16] J. A. Niestrawska, P. Regitnig, C. Viertler, T. U. Cohnert, A. R. Babu, and G. A. Holzapfel. The role of tissue remodeling in mechanics and pathogenesis of abdominal aortic aneurysms. *Acta Biomaterialia*, 88:149–161, 2019.

[17] M. A. Coady, J. A. Rizzo, G. L. Hammond, G. S. Kopf, and J. A. Elefteriades. Surgical intervention criteria for thoracic aortic aneurysms: a study of growth rates and complications. *Ann Thorac Surg*, 67(6):1922–1926, Jun 1999.

[18] C. S. Moskowitz and M. S. Pepe. Quantifying and comparing the predictive accuracy of continuous prognostic factors for binary outcomes. *Biostatistics*, 5(1):113–127, 01 2004.

[19] K. Kumar and L. S. Tuckerman. Parametric instability of the interface between two fluids. 279:49–68, 1994.